INVITED ARTICLE

Hydromechanics and Kinematics in Preferential Flow

Peter F. Germann

ABSTRACT:
Preferential flow covers macropore flow, nonequilibrium flow, and finger flow that are here exclusively approached with gravity-driven viscous flow. The basic unit is a water content wave whose two parameters are the wave's film thickness and its mainly vertical contact area per unit soil volume. The spatiotemporal wave properties depend on soil structure and on the intensity and duration of water input to the surface. Kinematic wave theory provides the mathematical tool for solving the analytical expressions. Three cases are the basic building blocks for approaching preferential flow: (*a*) single pulse, (*b*) a faster pulse trails a slower pulse, and (*c*) a faster pulse overtakes a slower pulse. Analytical procedures are presented for each case, and the potential of their applications is discussed. The analytical expressions and the superfluous representative elementary volume greatly facilitate preferential flow modeling.

Key Words: Darcy's law, permeable media, preferential flow, viscous flow

(Soil Sci 2018;183: 1–10)

Preferential flow (PF) in soils and similar permeable media is fast and gravity driven, and only a minor fraction of porosity participates in it. According to Jarvis et al. (2016), PF embraces unstable finger flow, macropore flow, and nonequilibrium flow. Hence, PF opposes ordinary flow that supposedly is stable and homogeneous and is in equilibrium with capillarity, that is, Richards' (1931) capillary flow (CF). Although opposing CF, most approaches to PF still circle around CF and have not yet evolved as independent flow types at levels comparable with CF. As presented here, however, viscous flow (VF) in permeable media is independent from CF, while capillarity appears merely as abstractor of water from VF. One-dimensional Darcy (1856) and two-dimensional Dupuit (1863)–Forchheimer approaches to flow in saturated permeable media as well as Hagen-Poiseuille (1846) flow in thin tubes are based on Newton's law of shear. The same principle is here applied to transient flow in partially water-saturated permeable media.

The article introduces first the concept of PF and its delineation from ordinary, that is, Richards' (1931) CF. It then presents the basic analytical expressions for VF in permeable media, whereas the more vivid kinematic-wave theory provides for the general mathematical solutions.

FACETS OF PREFERENTIAL FLOW AND ITS DISTINCTION FROM CAPILLARY FLOW

In the mid-19th century, physicians and physiologists got interested in the physics of blood flow: Hagen and Poiseuille (i.e., Poiseuille, 1846) applied Newton's (1729) law of shear to laminar flow in thin tubes. Moreover, numerous engineering projects triggered hydraulic approaches to flow in saturated permeable media: Darcy (1856), designing filters for the public water supply of Dijon, investigated one-dimensional flow in water-saturated permeable media, whereas Dupuit (1863) presented two-dimensional groundwater flow toward ditches and wells. Darcy's (1856) law and therefore Dupuit's (1863) approach are also based on Newton's law of shear as will be presented later on. Observations on water and solute transport in partially saturated soils were mainly based on lysimeter studies, like those of Lawes et al. (1882), for instance, who anticipated PF. They reported from the Rothamsted (UK) research station that "The drainage water of a soil may thus be of two kinds (1) of rainwater that has passed with but little change in composition down the open channels of the soil or (2) of the water discharged from the pores of a saturated soil." Further, "The respective proportions of direct and general drainage will vary much in different soils and under different circumstances." Also, "The two kinds of drainage water here mentioned differ much in composition, the direct channel drainage containing a much smaller proportion of soluble salts than is found in the true discharge from the soil."

Steps leading to this presentation include the lateral Br-sorption from macropores into tinier pores (Germann et al., 1984) that hints at the priority of PF over CF. Further, Germann (1986) concluded from infiltration-drainage measurements in the Coshocton lysimeters (Harrold and Dreibelbiss, l958; Kelley et al. 1975) that precipitations of 10 mm/d were sufficient for drainage to respond at the 2.5-m depth within 1 day. This results in wetting front velocities of approximately 2×10^{-5} m·s^{-1}. In the Kiel sand tank, Germann and al-Hagrey (2008) noted that the capillary potential ψ Pa collapsed close to atmospheric pressure during fast infiltration with a wetting front velocity of 3.3×10^{-5} m·s^{-1}. Nimmo (2012) suggested that PF also occurs under nonsaturated conditions, whereas Germann (2018a) provided experimental evidence of shock-like infiltration to occur in partially water-saturated permeable media under near-atmospheric pressure if the wetting shock front remains connected with the surface.

Preferential flow is usually associated with macropores, which implicitly call for the remaining pore space as micropores. The resulting pore space dichotomy requires demarcation. Jarvis et al. (2016), for instance, consider pores wider than approximately 300 to 500 μm as macropores. However, despite the majority of such qualitative demarcations, their quantification becomes essential when, out of opposition to CF, separate approaches to flow are to be applied to each pore class. In order to avoid all together the arbitrarily set thresholds and associated flow processes, the term *permeable media* is here given preference over porous media. Permeable media are thought of solids that are penetrated by voids such as fissures, cracks, and pores that are able to conduct water without restrictions on either the geometry or the volumetric share of the voids. Likewise, the proposed flow process does not require any *a priori* restriction with the exception of depending on low Reynolds numbers.

Despite the general recognition that PF is fast, there are few studies expressively dealing with its velocity. Ignoring capillarity, Beven and Germann (1981) approached gravity-driven and laminar macropore flow with VF according to Hagen-Poiseuille (1846). Beven and Germann (1981) also considered the theory of kinematic waves (KW) according to Lighthill and Witham (1955) as a suitable mathematical tool for dealing with VF along presumed macropores.

University of Bern, Bern, Switzerland.

Address for correspondence: Dr. Peter F. Germann, Geographisches Institut der Universität Bern, Hallerstrasse 12, CH-3012 Bern, Switzerland. E-mail: pf.germann@bluewin.ch

Financial Disclosures/Conflicts of Interest: None reported.

Received February 15, 2018.

Accepted for publication June 7, 2018.

ISSN: 0038-075X

DOI: 10.1097/SS.0000000000000226

The modeling study also revealed that the widest water-conducting paths dominate flow so strongly that already slightly narrower conduits markedly lose influence on flow. Germann (1985) demonstrated experimentally the feasibility of KW theory to the parameterization of PF in a block of polyester-cemented sand. Further investigations, for instance, those of Germann and al-Hagrey (2008), Hincapié and Germann (2009a, b; 2010), Germann and Karlen (2016), and Germann and Prasuhn (2017), led to the in situ experimental parameterization of VF. Nimmo's (2010) source-responsive free-surface film flow considers various elements within the same theoretical framework.

BASICS OF VISCOUS FLOW IN PERMEABLE MEDIA

Newton's Law of Shear

A rectangular pulse $P(q_S, T_B, T_E)$ provides the input to the soil surface, where q_S m·s^{-1} is its volume flux density (the subscript S refers to the surface), whereas T_B and T_E (both s) are the times of the pulse's beginning and ending. At T_B, P presumably initiates a water film gliding down the permeable medium. According to Fig. 1, the thickness F and the specific horizontal contact length L m·m^{-2} per cross-sectional area A m^2 of the permeable medium define the film, whereas f is the thickness variable, and df is the thickness of a layer (*lamina* in Latin, hence laminar flow). The solid-water interface (SWI) at $f = 0$ and the air-water interface (AWI) at $f = F$ confine the film. The film is accelerated by the specific weight $\rho \times g$ N·m^{-3}, where ρ (=1,000 kg·m^{-3}) is the water's density, and g (=9.81 m·s^{-2}) is acceleration due to gravity. The shear force φ Pa acts in the direction opposite to gravity, thus decelerating the film such that it moves downward with a constant velocity v_Wm·s^{-1} of the wetting shock front, whereas $z_W(t)$ is the wetting shock front's position as function of time. The term *wetting shock front* indicates the flow discontinuity at $z_W(t)$ that is initiated at T_B when P hits the soil surface. The z-coordinate points is positive from the surface down. The specific contact area of the film per volume of soil amounts to $L \times A \times z_W(t)/[A \times z_W(t)] = L$ m^2·m^{-3}.

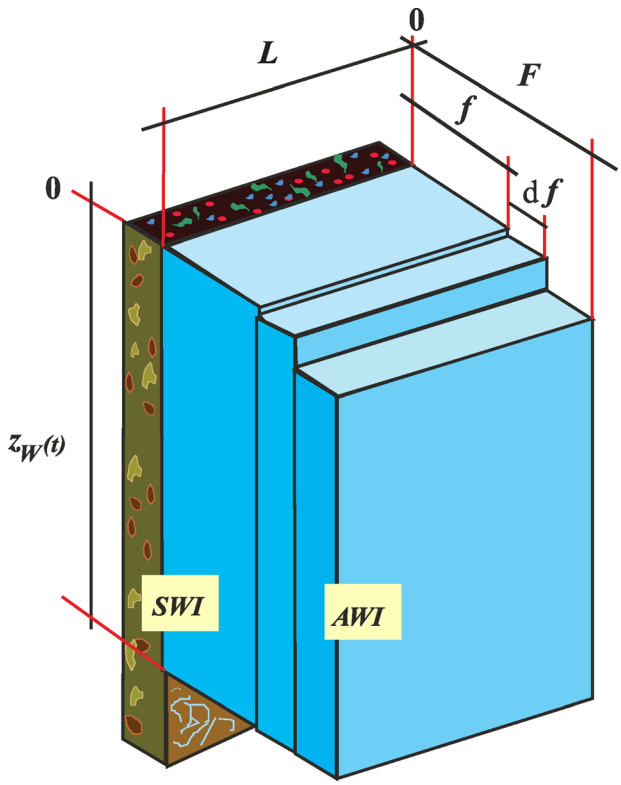

FIGURE 1. Film flow along a vertical plane. F is film thickness, f the thickness variable, and df the lamina thickness; $z_W(t)$ is the vertical position of the wetting shock front as function of time t; L is the specific contact line of the film per unit cross-sectional area; AWI and SWI are the interfaces between water and air as well as water and solid, respectively. Adapted with permission from Germann (2014). A color version of this figure is available in the online version of this article.

Momentum flux density at f is $\rho \times g \times z_W(t)$ Pa and is active in the direction of flow. Newton (1729) proposed the shear force φ as "The resistance, arising from the want of lubricity in the parts of a fluid, is, *caeteris paribus*, proportional to the velocity with which the parts of the fluid are separated from each other." Thus, momentum dissipation toward the SWI is proportionate to the velocity gradient at f, that is, dc/df s^{-1}, where the celerity c m·s^{-1} is the velocity of a particular film property. The factor of proportionality is the temperature-dependent kinematic viscosity η ($\approx$10 m^2·s^{-1}). Momentum dissipation toward the SWI produces the shear force $\varphi(f)$ Pa that acts in the opposite direction of momentum flux density due to gravity; $\varphi(f)$ balances the weight of the water film between f and F according to

$$\varphi(f)\cdot L = \eta\cdot\rho\cdot\left.\frac{\mathrm{d}c}{\mathrm{d}f}\right|_f\cdot L = \rho\cdot g\cdot L\cdot(F-f) \qquad [1]$$

The center part of Eq. [1] represents the dissipation of momentum due to the celerity gradient of dc/df at f. The right hand side of Eq. [1] represents the weight of the water film with the volume of $L \times (F - f)$. The dynamic force balance in Eq. [1] produces the constant celerity c at f. Simplifying Eq. [1], separating the variables and integrating it from $f = 0$ to $f = F$ under the consideration of $c(0) = 0$ (the nonslip condition) yield the parabolic celerity profile in the horizontal f direction as

$$c(f) = \frac{g}{\eta}\cdot\left(F\cdot f - \frac{f^2}{2}\right) \qquad [2]$$

Viscous Flow in Permeable Media

The pulse P hitting the surface at $t = T_B$ releases a water content wave (WCW) at $z = 0$. Figure 2 depicts the WCW that envelops the spatiotemporal distribution of the mobile water content, $w(z,t)$ m^3·m^{-3}. During input, $T_B \le t \le T_E$, the WCW assumes the shape of a water film according to Fig. 1. Both parameters, F and L, are due to P and the actual specific properties of the permeable medium. Cessation of P at $t = T_E$ initiates the film's thinning.

During infiltration, that is, $T_B \le t \le T_E$, the specific volume V_{WCW} m of the film as function of time is

$$V_{WCW}(t) = F\cdot L\cdot z_W(t) = q_S\cdot(t - T_B) \qquad [3]$$

Under the auspice of P and after infiltration has ceased, that is, $t > T_E$, the total and maximum specific water volume of the WCW remains at $V_{tot} = q_S \times (T_E - T_B)$ if the WCW neither gains nor loses water. The mobile water content w m^3·m^{-3} amounts to

$$w = F\cdot L \qquad [4]$$

The differential volume flux density at f is

$$\mathrm{d}q|_f = L\cdot\mathrm{d}f\cdot c(f) \qquad [5]$$

Its integration from the SWI to the AWI leads to the volume flux density q_Sm·s^{-1} of the film as

$$q_S = F^3\cdot L\cdot\frac{g}{3\cdot\eta} = {w_S}^3\cdot\frac{g}{3\cdot L^2\cdot\eta} \qquad [6]$$

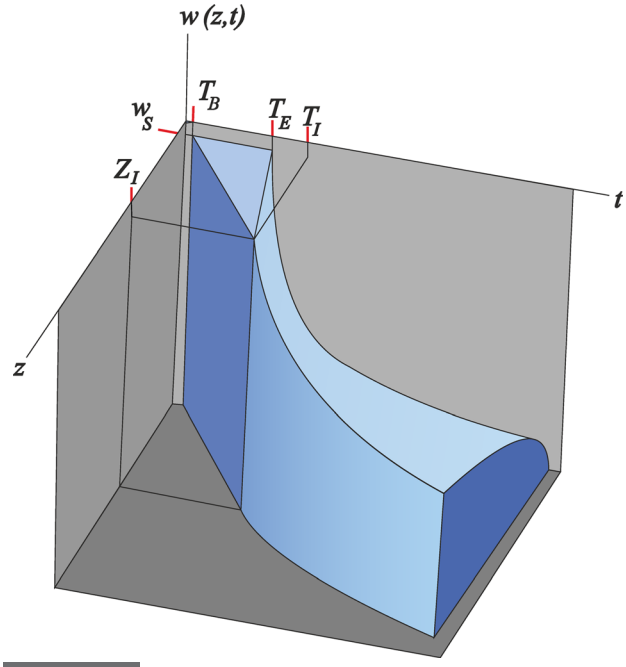

FIGURE 2. Schematic representation of a WCW. $w(z,t)$ is mobile water content, t and z are the axes of time and depth; T_B and T_E indicate beginning and ending of the water pulse $P(q_S, T_B, T_E)$ that hits the surface at $z = 0$; T_I and Z_I are time and depth of the wetting front intercepting the draining front. The line from (0, 0) to (Z_I, T_I), and beyond represents the position of the wetting shock front, $z_W(t)$, whereas the line from (0, T_E) to (Z_I, T_I) gives the position of the draining front, $z_D(t)$. Adapted with permission from Germann (2014). A color version of this figure is available in the online version of this article. full color online

From the volume balance follows the velocity v_W m·s^{-1} of the wetting shock front as

$$v_W = \frac{q_S}{w_S} = \frac{z_W(t)}{t - T_B} = F^2 \cdot \frac{g}{3 \cdot \eta} \quad [7]$$

Thus, the force balance, Eq. [1], leads to a constant velocity $v_W = \mathrm{d}z_W(t)/\mathrm{d}t$ m·s^{-1} of the film's wetting shock front. Laminar VF applies to Reynolds numbers $Re < \approx 3$, with Re defined as

$$Re = \frac{F \cdot v}{\eta} = \frac{F^3 \cdot g}{3 \cdot \eta^2} = \left(\frac{3 \cdot v^3}{g \cdot \eta}\right)^{1/2} \leq 3 \quad [8]$$

that limits the maximal tolerable film thickness F to approximately 100 μm.

Viscous flow occurs in unsaturated permeable media, that is, $w < (\varepsilon - \theta)$, where ε and θ (both m^3·m^{-3}) are porosity and antecedent volumetric water content of the medium, respectively. According to Eq. [1], the pressure gradient from VF is $\Delta p/(\Delta z \times \rho \times g) = 1$. Darcy's law for vertical flow is based on the same principles but for saturated media with $w = (\varepsilon - \theta)$ and the pressure gradient of $\Delta p/(\Delta z \times \rho \times g) > 1$. The particular case is the hydraulic conductivity K m·s^{-1} amounting to q_S according to Eq. [6] under the special conditions of $w = (\varepsilon - \theta)$ and $\Delta p/(\Delta z \times \rho \times g) = 1$.

The cessation of input at T_E causes the mobile water content at the surface to jump from w_S to 0 and the film thickness from F to 0. Therefore, the jump releases at once the rear ends of all the laminae that continue to glide one over the other. Each rear end moves with the celerity c (f) that reduces with decreasing distance from the SWI according to Eq. [2]. Thus, the film starts to flatten, and the spatiotemporal distribution of the mobile water content $w(z,t)$ of a WCW after $t > T_E$ becomes

$$w(z,t) = L \cdot \left(\frac{\eta}{g}\right)^{1/2} \cdot z^{1/2} \cdot (t - T_E)^{-1/2} \quad [9]$$

(Germann and Karlen, 2016). The outermost lamina at F moves the fastest with the celerity c_D m·s^{-1} of the draining front (indexD), thus

$$c_D = \frac{\mathrm{d}q_S}{\mathrm{d}w} = 3 \cdot v_W \quad [10]$$

Equation [10] applies to all the lamina originating at F during $T_B \leq t \leq T_E$; however, the slower moving wetting shock front, Eq. [7], continuously intercepts them.

Because of $c_D = 3\ v_W$, the wetting shock front that was released at T_B intercepts at depth and time Z_I m and T_Is, the faster-moving draining front that was later released at T_E. Depth and time of interception follow from the two relationships of $Z_I = (T_I - T_B) \cdot v_W$ and $Z_I = (T_I - T_E) \cdot c_D$ that are to be solved for Z_I and T_I, yielding

$$Z_I = \frac{c_D}{2} \cdot (T_E - T_B) \quad [11]$$

$$T_I = \frac{1}{2} \cdot (3 \cdot T_E - T_B) \quad [12]$$

where T_I depends only on T_B and T_E.

After $t \geq T_I$ and beyond $z \geq Z_I$, the wetting shock front forms a crest (index CR) that moves downward with the decreasing velocity of

$$v_{CR}(t) = v_W \cdot \left(\frac{T_E - T_B}{2 \cdot (t - T_E)}\right)^{2/3} \quad [13]$$

The mobile water content at the crest declines with time according to

$$w_{CR}(t) = w_S \cdot \left(\frac{T_E - T_B}{2 \cdot (t - T_E)}\right)^{1/3} \quad [14]$$

Equations [13] and [14] are according to Germann (2014) and to Germann and Karlen (2016). The following three sections present the three projections of the WCW, Fig. 2, onto the w-z, the w-t, and the z-t planes.

PROFILES OF MOBILE WATER CONTENTS $w(z,\tau)$

The profiles of $w(z,\tau)$ are now considered that appear as projections of the WCW onto the w-z plane in Fig. 2. Three intervals are to be distinguished: (i) $[T_B \leq \tau_1 \leq T_E]$, (ii) $[T_E \leq \tau_2 \leq T_I]$, and (iii) $[\tau_3 \geq T_I]$. Interception time T_I is according to Eq. [12]. Figure 3 provides examples of $w(z,\tau)$ during the three periods and at T_I.

Interval (i): $T_B \leq \tau_1 \leq T_E$

The position $z_W(\tau_1)$ of the wetting shock front is

$$z_W(\tau_1) = v_W \cdot (\tau_1 - T_B) \quad [15]$$

whereas the mobile water content is

$$w(z, \tau_1) = w_S = F \cdot L \quad [16]$$

Steady state prevails during this interval. Line $\tau_1 / T_I = 0.24$ in Fig. 3 illustrates $w(z,\tau_1)$.

Interval (ii): $T_E \leq \tau_2 \leq T_I$

The position of the wetting shock and draining fronts, $z_W(\tau_2)$ and $z_D(\tau_2)$, are

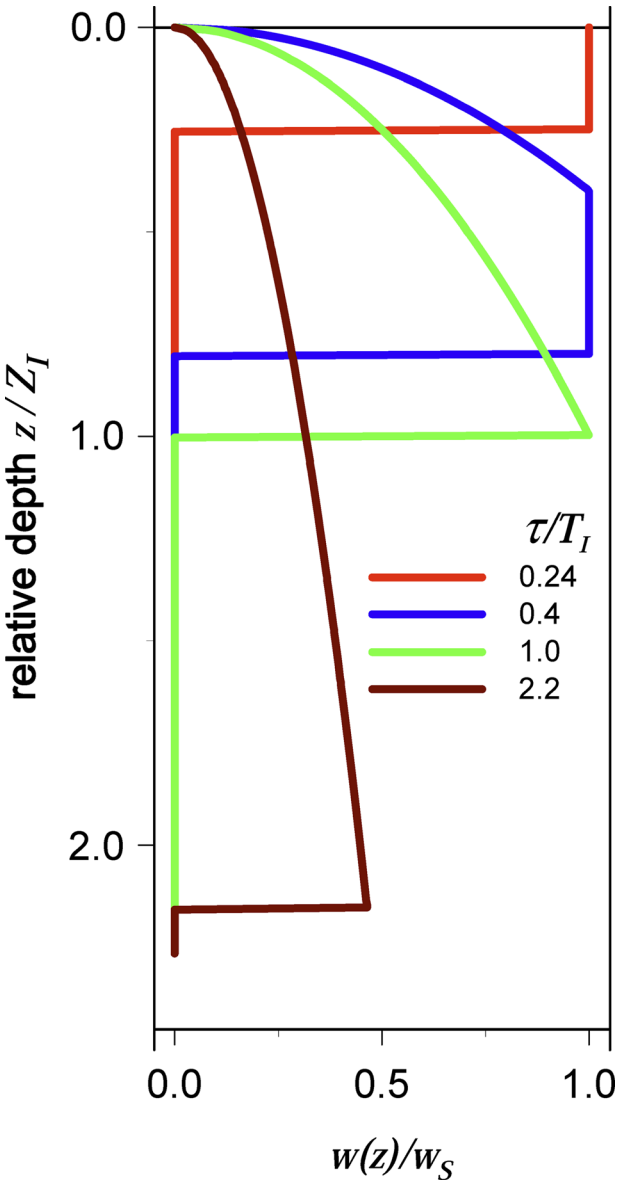

FIGURE 3. Profiles of relative mobile water contents $w(z)/w_S$ at the four relative times τ/T_I of $\tau_1/T_I = 0.24$, $\tau_2/T_I = 0.4$, $T_I = 1.0$, and $\tau_3/T_I = 2.2$. Adapted with permission from Germann (2014). A color version of this figure is available in the online version of this article.

$$z_W(\tau_2) = v_W \cdot (\tau_2 - T_B) \quad [17]$$

$$z_D(\tau_2) = c_D \cdot (\tau_2 - T_E) \quad [18]$$

The mobile water content $w(z,\tau_2)$ in the depth range of $0 < z < z_D(\tau_2)$ amounts to

$$w(z,\tau_2) = L \cdot \left(\frac{\eta}{g}\right)^{1/2} \cdot z^{1/2} \cdot (\tau_2 - T_E)^{-1/2} \quad [19]$$

In section $z_D(\tau_2) < z < z_W(\tau_2)$, it is

$$w(z,\tau_2) = w_S \quad [20]$$

Line $\tau_2/T_I = 0.4$ in Fig. 3 illustrates $w(z,\tau_2)$

Interval (iii): $\tau_3 \geq T_I$

The position of the wetting shock front $z_W(\tau_3)$ after interception becomes

$$z_W(\tau_3) = c_D \cdot \left(\frac{T_E - T_B}{2}\right)^{2/3} \cdot (\tau_3 - T_E)^{1/3} \quad [21]$$

(Germann and Karlen, 2016). The mobile water content in the section of $0 < z < z_W(\tau_3)$ amounts to

$$w(z,\tau_3) = L \cdot \left(\frac{\eta}{g}\right)^{1/2} \cdot z^{1/2} \cdot (\tau_3 - T_E)^{-1/2} \quad [22]$$

Line $\tau_3/T_I = 2.2$ in Fig. 3 illustrates $w(z,\tau_3)$.

Discussion of *w* Profiles

So far, the section considered only the mobile water contents $w(z,\tau_{1,2,3})$. The respective volume flux densities follow from Eq. [8]. Water balance calculations of the entire WCW require $w(z,t)$ profiles. Germann and Prasuhn (2017) provide examples of VF propagations in a weighing lysimeter.

TIME SERIES OF MOBILE WATER CONTENTS $w(\zeta,t)$

This section considers time series of $w(z,t)$ that show as projections of the WCW onto the w-t plane in Fig. 2. Two sections are to be considered: (i) $[0 \leq \zeta_1 \leq Z_I]$ and (ii) $[\zeta_2 \geq Z_I]$, whereas the interception depth, Z_I, is according to Eq. [11].

Section (i): $0 \leq \zeta_1 \leq Z_I$

According to Eqs. [7] and [10], the time lapses $t_W(\zeta_1)$ and $t_D(\zeta_1)$ for the wetting shock and draining fronts to arrive at ζ_1 are

$$t_W(\zeta_1) = T_B + \frac{\zeta_1}{v_W} \quad [23]$$

$$t_D(\zeta_1) = T_E + \frac{\zeta_1}{c_D} \quad [24]$$

The associated mobile water contents amount to

$$T_B \leq t \leq t_W(\zeta_1) : w(\zeta_1,t) = 0 \quad [25]$$

$$t_W(\zeta_1) \leq t \leq t_D(\zeta_1) : w(\zeta_1,t) = w_S \quad [26]$$

Equation [26] indicates steady state, that is, piston flow.

$$t \geq t_D(\zeta_1) : w(\xi_1,t) = w_S \cdot \left(\frac{t_D(\zeta_1) - T_E}{t - T_E}\right)^{1/2} \quad [27]$$

Lines $\zeta_1/Z_I = 0.4$ and 0.85 in Fig. 4A represent Eqs. [23] to [27], whereas the corresponding lines in Fig. 4B show the associated volume flux densities.

Section (ii): $\zeta_2 \geq Z_I$

The WCW reduces to a crested wave. According to Eq. [21], the time $t_{CR}(\zeta_2)$ lapsed for the wetting shock to move to ζ_2 is

$$t_{CR}(\zeta_2) = T_E + \left(\frac{\zeta_2}{c_D}\right)^3 \cdot \left(\frac{T_E - T_B}{2}\right)^{-2} \quad [28]$$

The mobile water content at the crested wetting shock front amounts to

$$w_{CR}(\zeta_2,t) = w_S \cdot \left(\frac{T_E - T_B}{2 \cdot (t - T_E)}\right)^{1/3} \quad [29]$$

Thus, the associated mobile water contents amount to

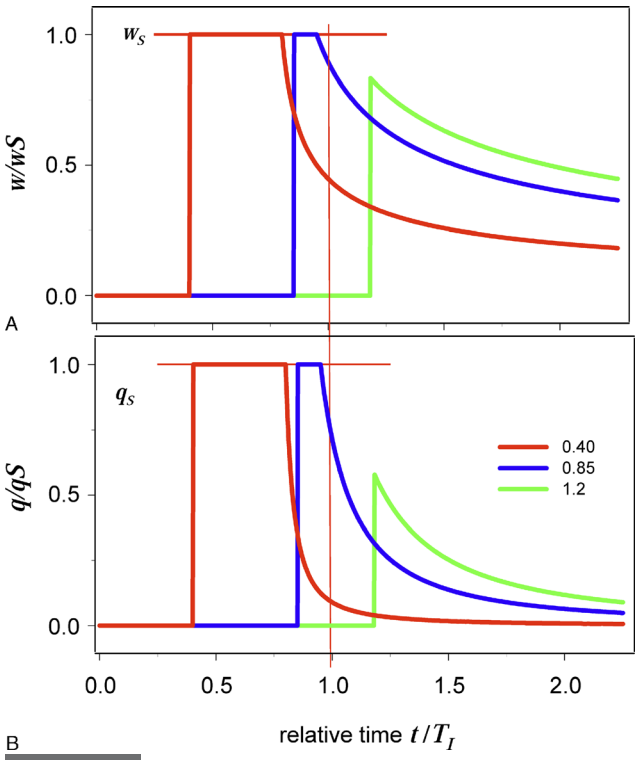

FIGURE 4. Series of mobile water contents and associated volume flux densities. A, Relative mobile water content, w/w_S, versus relative time t/T_I at relative depths of $\zeta_1/Z_I = 0.4$ and 0.85, and $\zeta_2/Z_I = 1.2$. B, Relative volume flux density, q/q_S, versus relative time t/T_I at the same relative depths as Fig. 4A. Adapted with permission from Germann (2014). A color version of this figure is available in the online version of this article.

$$T_B \le t \le t_{CR}(\zeta_2) : w(\zeta_2, t) = 0 \quad [30]$$

$$t \ge t_{CR}(\zeta_2) : w(\zeta_2, t) = w_{CR}(\zeta_2, t) \cdot \left(\frac{t_{CR}(\zeta) - T_E}{t - T_E} \right)^{1/2} \quad [31]$$

Line z2/Z_I = 1.2 in Fig. 4A represents Eqs. [28] to [31]. Figure 4B depicts the volume flux densities that follow from the application of Eq. [6] to the mobile water contents.

Discussion of *w* Time Series

Time series of w at particular depths are the favorite mode for in situ estimations of F and L, for instance, with rapid θ measurements using time-domain reflectometry equipment (Germann, 2018b; Germann and Karlen, 2016). In order to reduce the number of variables, experimenters are advised to restrict the measurements to the depth range of $0 \le z \le Z_I$. The requirement is easy to achieve by simply extending the duration of experimental input long enough, as Eqs. [11] and [12] reveal.

KINEMATIC WAVE THEORY: THE TRAJECTORIES OF MOBILE WATER CONTENTS IN THE *z-t* PLANE

So far, a single rectangular pulse P was considered as input to the permeable medium that was routed according to the rules of VF. However, a more realistic scenario to natural processes requires the temporal variation of input. For that, any water input to the surface as function of time is divided into a series of n rectangular pulses $P(T_B, T_E, q_S)_j$ with $1 \le j \le n$ that need to be routed according to VF. The selection of $(T_B, T_E)_j$ allows for smooth adjustment of the VF approach to reality. A straightforward procedure of pulse routing evolves from the projection of the WCW onto the z-t plane leading to the temporal positions of $w(z,t)$ and, subsequently, of $q(z,t)$. The procedure draws from Lighthill and Witham (1955), who developed the KW theory for flows of water in long uniform channels and for traffic flows. Kinematic wave permits the routing of pulse series, in those each pulse carries its own duration and $w_S(q_S)$ value. The temporal positions of w follow from relationships that depend exclusively on the volume balance, hence, the adjective "kinematic". The resulting analytical equations greatly facilitate modeling of PF as laminar VF. Pulse routing relies on three categories of WCW projections onto the z-t plane: (i) The already known wetting- and draining-front positions, (ii) the characteristics as straight-lined trajectories of properties, such as draining fronts, which move with constant celerities, and (iii) the interception function.

Kinematic wave theory applies to VF under the premises of low Reynolds numbers, Eq. [8], and of

$$q(w) = b \cdot w^3 \quad [32]$$

where the conductance b m·s^{-1} amounts to

$$b = \frac{g}{3 \cdot \eta \cdot L^2} \quad [33]$$

Equation [32] is referred to as the VF function from which follows that

$$w = \left(\frac{q}{b} \right)^{1/3} \quad [34]$$

Further, VF in a particular permeable medium presumably follows the same paths independently from the input rate. This requires a constant specific surface area L, that is,

$$dL/dq = 0 \quad [35]$$

The constraint of Eq. [35] is referred to as macropore-flow restriction that leads to $db/dq = 0$ in Eqs. [32] to [34]. From the volume balance follow the wetting front velocity as

$$v_W = \frac{q_S}{w_S} = b \cdot {w_S}^2 \quad [36]$$

whereas the celerity of the draining front is

$$c_D = \frac{dq_S}{dw_S} = 3 \cdot b \cdot {w_S}^2 \quad [37]$$

Moreover, the macropore-flow restriction relates the velocity of the wetting shock front with the volume flux density of input as

$$v_W(q_S) = b^{1/3} \cdot {q_S}^{2/3} \quad [38]$$

Figure 5 illustrates the VF function, Eq. [32], and KW properties under the auspice of Eq. [35]. Thus, the slopes of lines (4) and (5) in Fig. 5 depict $v_{W1,2}$ for two mobile water contents w_1 and $w_2 > w_1$ or their two corresponding volume flux densities q_1 and $q_2 > q_1$.The slopes of the tangents to $q(w_1,w_2)$, lines (2) and (3) in Fig. 5 represent $c_{D1,2}$, where generally $c_D = 3 \times v_W$.

Three canonical cases emerge as the basic entity for approaching VF with KW theory:

(i) routing of a single pulse;

(ii)) routing of a faster pulse with higher-volume flux density that trails a slower pulse with lower-volume flux density;

(iii) routing of a faster pulse with higher-volume flux density that superimposes (overtakes) a slower pulse with lower-volume flux density.

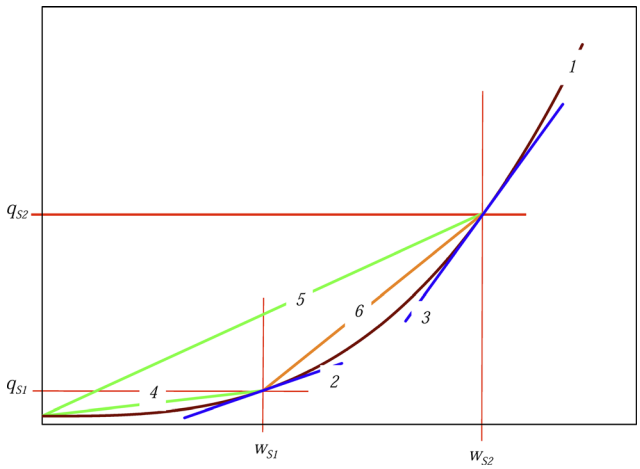

FIGURE 5. Kinematic flow relationships. Volume flux densities q_{S1} (w_{S1}) and q_{S2}(w_{S2}) of $w_{S1} < w_{S2}$ under the macropore flow restriction. Line (1): volume flux density versus mobile water content $q(w)$; lines (2) and (3): the slopes of the tangents represent the draining front celerities c_{D1} and c_{D2}; lines (4) and (5): the slopes of the chords q/w represent the wetting shock front velocities v_1 and v_2; line (6): the slope of the chord represents the celerity c_{J12} of the jump from w_{S2} to w_{S1}. Adapted with permission from Germann (2014). A color version of this figure is available in the online version of this article.

Propagation of a Single Pulse

Let's consider one pulse $P(q_S, T_B, T_E)$, hence, with w_S according to Eq. [34]. The interception time T_I separates pulse routing in an early interval, $T_B \le \tau_1 \le T_I$, and in late interval, $\tau_2 \ge T_I$, whereas $q(z,t)$ or $w(z,t)$ are the WCW properties to be routed in the two intervals.

(i) Interval $T_B \le \tau_1 \le T_I$

Interception depth and time are the result from the same procedure that led to Eqs. [11] and [12] as Fig. 6 illustrates: line (1) represents the position of the wetting shock front, and line (3) the characteristic (i.e., trajectory) of the draining front (for clarity, Fig. 6 omits labeling Z_I). The figure also compares the wetting shock front depth of a pulse produced by a smaller mobile water content $w_{S1/2}$ (thin lines) with the wetting shock front depth of a pulse produced by a greater mobile water content w_S (heavy lines), thus demonstrating the exclusive dependence of T_I on T_B and T_E and independent from w_S and q_S.

During τ_1, all the laminae of P move along their characteristics that are intercepted by the slower-moving wetting shock front. The slopes of the characteristics express the laminae's celerities as lines (2) and (3) in Fig. 6 as well as lines (2) and (3) in Fig. 5 illustrate. The mobile water content along the wetting shock front is constant at w_S.

(ii) Interval $\tau_2 \ge T_I$

The cessation of input at T_E releases at once all the rear ends of the laminae, whereas the lamina at F, Figs. 1 and 2, moves the fastest with $c_D = c(f)$, Eq. [2], along the characteristic of line (3) in Fig. 6. Each rear end moves with the celerity $c(f)$ that decreases with decreasing distance f from the SWI (Fig. 1). Thus, the film starts to collapse, the WCW flattens, and the characteristics spread as, for instance, line (4) in Fig. 6 indicates. Spreading of the characteristics implies deceleration of the wetting shock front whose position $z_W(\tau_2)$ is, in analogy with Eq. [21],

$$z_W(\tau_2) = c_D \cdot \left(\frac{T_E - T_B}{2}\right)^{2/3} \cdot (\tau_2 - T_E)^{1/3} \qquad [39]$$

The mobile water content along the wetting shock front is similar to Eq. [29], while $w(z,t)$ in the area confined by the characteristic of the draining front, line (3) in Fig. 6 and Eq. [18], and the wetting shock front, Eq. [39], are according to Eq. [27].

Germann (2014) demonstrated that the straight-lined position of the wetting shock front, $z_W(\tau_1)$, prior to T_I, line (1) in Fig. 6, generally touches tangentially at the interception point (Z_I/T_I) the curved-lined position $z_W(\tau_2)$ of the wetting shock front after T_I, line (5) in Fig. 6. Thus Eqs. [21] and [39] express the pulse's interception function that is completely determined by c_D, Eq. [10], and the pulse duration $[T_E - T_B]$. Accordingly, line (5) in Fig. 6 represents the potential position of interception (Z_I/T_I) prior to T_I that turns into the effective wetting shock front position $z_W(\tau_2)$ after T_I. The interception function facilitates modeling.

Propagation of a Faster Pulse With Higher-Volume Flux Density Trailing a Slower Pulse With Lower-Volume Flux Density

Let's now consider two pulses $P_1(q_{S1}, T_{B1}, T_{E1})$ and $P_2(q_{S2}, T_{B2}, T_{E2})$, where $q_{S2} < q_{S1}$, $w_{S2} < w_{S1}$, and $T_{E1} = T_{B2}$; thus, P_1 trails P_2. As shown in Fig. 7, the arrangement requires three interception depths and times that are

T_{I1}, when the wetting shock front of P_1 intercepts its draining front, lines (1) and (2) in Fig. 7;

T_{I12}, when the wetting shock front of P_1 intercepts the draining front of the first lamina of P_2, as expressed by its characteristic, line (3) in Fig. 7; and

T_{I2}, when the straight wetting shock front of P_2 intercepts the draining from the last lamina of P_2 as shown with its characteristic, line (4) in Fig. 7. Lines (3) and (4) are parallels.

The following presents the procedures of determining the three interception times and depths, the wetting shock front depths during the four intervals of (i) $[T_B \le \tau_1 \le T_{I1}]$, (ii) $[T_{I1} \le \tau_2 \le T_{I12}]$, (iii) $[T_{I12} \le \tau_3 \le T_{I2}]$, (iv) $[\tau_4 \ge T_{I2}]$, and the associated mobile water contents.

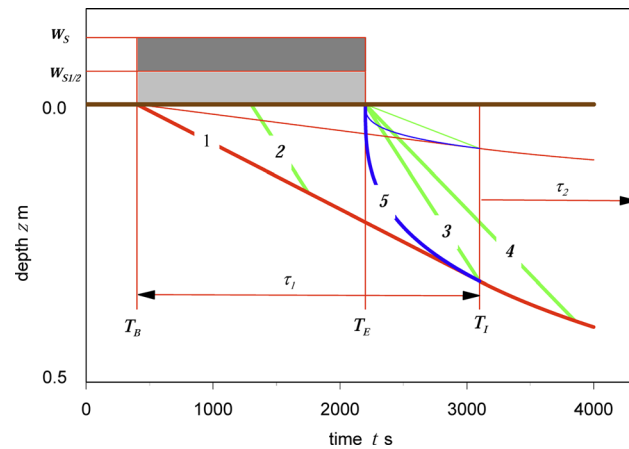

FIGURE 6. Wetting front trajectory, characteristics, and interception function of two single pulses. w_S and $w_{S1/2}$ are the mobile water contents resulting from two pulses with the same beginning at T_B and ending at T_E. The heavy lines are related to w_S, whereas the thin lines represent $w_{S1/2}$. The wetting front, line (1), cuts the characteristic of the draining front, line (3) at the time of interception, T_I; line (2) is the characteristic of a arbitrary lamina released at time $t < T_E$ that is parallel to line (3); line (4) is the characteristic of an arbitrary lamina that was released at $f < F$ at $t = T_E$; line (5) is the interception function (that turns into the curved temporal position of the wetting shock front during τ_2); the interception time T_I separates the periods τ_1 and τ_2, whereas it is independent from the water contents of the pulses. (The depth Z_I corresponding to T_I is not marked for clarity reasons.) Adapted with permission from Germann (2014). See also Fig. 5 for the KW expressions. A color version of this figure is available in the online version of this article.

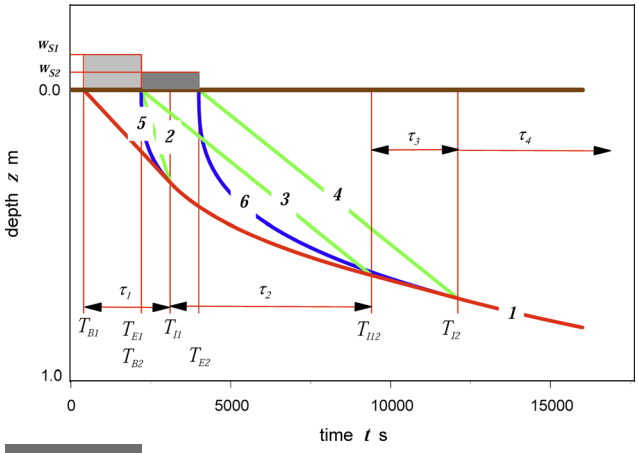

FIGURE 7. Wetting front trajectory, characteristics, and interception function of the faster pulse P_1 trailing the slower pulse P_2. Line (1) gives the temporal position of the wetting front during the four periods τ_1 to τ_4 between the beginning of P_1 at T_{B1}, the interception times T_{I1}, T_{I12}, T_{I2}, and after T_{I2}; line (2) is the characteristic of the draining front from P_1; lines (3) and (4) are the parallel characteristics of P_2; lines (5) and (6) are the interception functions (that turn into the curved sections of the wetting shock fronts during the respective periods τ_2 and τ_4.) Adapted with permission from Germann (2014). See also Fig. 5 for the KW expressions. A color version of this figure is available in the online version of this article. full color online

(i) Interval $T_B \le \tau_1 \le T_{I1}$

The wetting shock front of P_1, line (1) in Fig. 7, intercepts P_1's draining front, line (2) in Fig. 7, at T_{I1} and Z_{I1} that are, in accord with Eqs. [11] and [12],

$$T_{I1} = \frac{1}{2}\cdot(3\cdot T_{E1} - T_{B1}) \qquad [40]$$

$$Z_{I1} = \frac{c_{D1}}{2}\cdot(T_{E1} - T_{B1}) \qquad [41]$$

where c_{D1} expresses the celerity of P_1's draining front that started moving at T_{E1}. During τ_1, the mobile water content at the wetting front amounts to w_{S1} that is maintained between the wetting and draining fronts, lines (1) and (2) in Fig. 7. After passing of the draining front, the mobile water content reduces in analogy to Eq. [27].

(ii) Interval $T_{I1} \le \tau_2 \le T_{I12}$

Line (5) in Fig. 7 shows the interception function of P_1 that continues, in analogy with Eq. [21], as curved wetting shock front during τ_2 as

$$z_W(\tau_2) = c_{D1}\cdot\left(\frac{T_{E1} - T_{B1}}{2}\right)^{2/3}\cdot(\tau_2 - T_{E1})^{1/3} \qquad [42]$$

that is, line (1) in Fig. 7. However, only the rear ends of P_1's laminae in the mobile water content range of $w_{S1} > w > w_{S2}$ arrive at the wetting front, whereas those of $w < w_{S2}$ do not show because P_2 sustains w_{S2}. While P_1 trails P_2, the first lamina of P_2 moves with the celerity c_{D2} (i.e., P_1 lubricates P_2). Thus, the wetting shock front $z_W(\tau_2)$, Eq. [42], intercepts at (Z_{I12}/T_{I12}), the first lamina of P_2 whose characteristic is line (3) in Fig. 7. Equating the temporal position of $c_{D2}\times(\tau_2 - T_{B2})$ of P_2's first lamina with Eq. [42] and solving for time lead to the interception time and depth of

$$T_{I12} = T_{B2} + \left(\frac{c_{D1}}{c_{D2}}\right)^{3/2}\cdot\frac{(T_{B2} - T_{B1})}{2} \qquad [43]$$

$$Z_{I12} = c_{D2}\cdot\left(\frac{c_{D1}}{c_{D2}}\right)^{3/2}\cdot\frac{(T_{B2} - T_{B1})}{2} \qquad [44]$$

During τ_2, the mobile water content at the wetting shock front gradually reduces from w_{S1} to w_{S2} in accord with Eq. [29]

$$w(\tau_2) = w_{S1}\cdot\left(\frac{T_{E1} - T_{B1}}{2\cdot(\tau_2 - T_{E1})}\right)^{1/3} \qquad [45]$$

From the surface to the wetting front, the mobile water content reduces from w_{S1} to w_{S2} between the characteristic of P_1's draining front, line (2), and P_2's first lamina, line (3) in Fig. 7, where $w(\tau_2)$ from Eq. [45] replaces w_{CR} in Eq. [29].

(iii) Interval $T_{I12} \le \tau_3 \le T_{I2}$

The laminae of P_2 glide one over the other with constant celerity that results in the constant wetting shock front velocity of $v_{W2} = c_{D2}/3$. Thus, the temporal wetting shock front depth during τ_3 becomes

$$z_W(\tau_3) = v_{W2}\cdot(\tau_3 - T_{B2a}) \qquad [46]$$

where the time offset T_{B2a}s indicates the apparent earlier beginning of P_2 that accounts for P_1 trailing P_2 (i.e., P_2 pick-a-packing on P_1). Thus, the wetting front of P_2 appears earlier at Z_{I12} than if it were released from and moving as a single pulse. Thus, $T_{B2a} < T_{B2}$, and

$$T_{B2a} = T_{I12} - \frac{Z_{I12}}{v_{W2}} \qquad [47]$$

The time offset T_{B2a} affects only the temporal position of the wetting front, but by no means does it affect the WCWs' volume balances. Also, the characteristic of P_1's draining front, line (2) in Fig. 7, is steeper than the characteristics of P_2's laminae, lines (3, 4) in Fig. 7. This again is due to P_1's trailing of P_2. (See also the corresponding slopes of lines (5) and (4) on $q(w)$ in Fig. 5 that indicate the slowdown of the fronts when switching from w_{S2} to w_{S1}.) During τ_3, the draining front of P_2 moves along the characteristic $z_{D2}(\tau_3)$, line (4) in Fig. 7, that is

$$z_{D2}(\tau_3) = c_{D2}\cdot(\tau_3 - T_{E2}) \qquad [48]$$

Equating Eq. [46] with Eq. [48] and solving for τ_3 lead to the interception time and depth of

$$T_{I2} = \frac{1}{2}\cdot\left(\frac{Z_{I12}}{v_{W2}} + 3\cdot T_{E2} - T_{I12}\right) \qquad [49]$$

$$Z_{I2} = \frac{3}{2}\cdot[Z_{I12} + v_{W2}\cdot(T_{E2} - T_{I12})] \qquad [50]$$

During τ_3, the mobile water content at the wetting front amounts to w_{S2}. It remains at w_{S2} between the characteristics of P_2's first and last laminae, lines (3) and (4) in Fig. 7.

(iv) Interval $\tau_4 \ge T_{I2}$

In analogy with Eqs. [21] and [42], during τ_4 and below Z_{I2}, the wetting front $z_W(\tau_4)$ moves along line (1) in Fig. 7, as

$$z_W(\tau_4) = c_{D2}\cdot\left(\frac{T_{E2}-T_{B2a}}{2}\right)^{2/3}\cdot(\tau_4-T_{E2})^{1/3} \quad [51]$$

The mobile water content at the wetting front during τ_4 amounts to

$$w(\tau_4) = w_{S2}\cdot\left(\frac{T_{E2}-T_{B2}}{2\cdot(\tau_4-T_{E2})}\right)^{1/3} \quad [52]$$

where $w(\tau_4)$ from Eq. [52] replaces w_{CR} in Eq. [29]. The mobile water content in the spatiotemporal range beyond the characteristic of the last lamina of P_2 (i.e., to the right of line (4) in Fig. 7) follows from Eq. [27], where w_{S2} replaces w_S.

All volume flux densities are functions of the mobile water contents according to Eq. [32]. The water balance of the two pulses P_1 and P_2 at any given time $t > T_{B1}$ equates the total volume of infiltrated water with the total increase of the mobile water content from the soil surface to the wetting shock front depth at $z_W(t)$. For example, the total volume of the infiltrated water must be equal to the total increase of the mobile water content from the surface to the wetting shock front depth after its interception of the second draining front at depths $z_W(\tau_4)$, thus

$$q_{S1}\cdot(T_{E1}-T_{B1}) + q_{S2}\cdot(T_{E2}-T_{B2}) = \int_0^{z_W(\tau 4)} w(z,t)\,dz = \frac{2}{3}\cdot L\cdot\left(\frac{\eta}{g}\right)^{\frac{1}{2}}\cdot(\tau_4-T_{E2})\cdot z_W(\tau_4)^{\frac{3}{2}} \quad [53]$$

The right-hand side of Eq. [53] results from integrating the water content profile, Eq. [22], where the depth $z_W(\tau_4)$ follows from Eq. [51].

Propagation of a Faster Pulse With Higher-Volume Flux Density That Superimposes (Overtakes) a Slower Pulse With Lower-Volume Flux Density

Let's consider two pulses $P_1(q_1, T_{B1}, T_{E1})$ and $P_2(q_2, T_{B2}, T_{E2})$, such that $q_{S2} > q_{S1}$, $w_{S2} > w_{S1}$, and $T_{E1} = T_{B2}$. Mass balance requires the discontinuity of the jump from P_1 to P_2 to move with the celerity of

$$c_{J12} = \frac{q_{S2}-q_{S1}}{w_2-w_1} \quad [54]$$

$m\cdot s^{-1}$ (Lighthill and Witham, 1955). Line (2) in Fig. 8 shows the characteristic of the jump. (The slope of line (6) in Fig. 5 represents c_{J12}.) Figure 8 suggests two interception times:

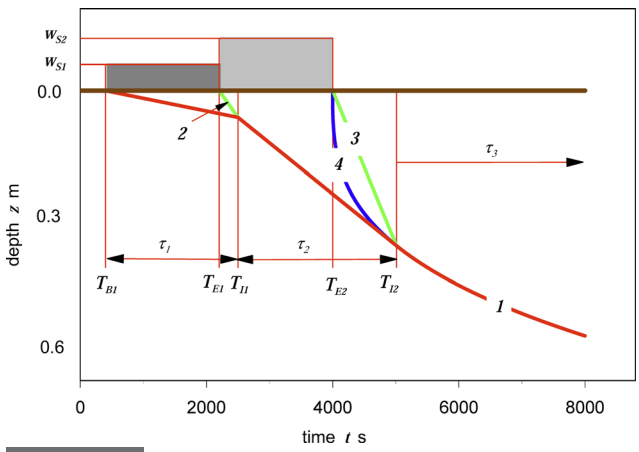

FIGURE 8. Wetting front trajectory, characteristics, and interception function of the faster pulse P_2 superimposing (overtaking) the slower pulse P_1. Line (1) gives the temporal position of the wetting shock front during the three periods τ_1 to τ_3 between the beginning of P_1 at T_{B1}, the interception times T_{I1}, T_{I2}, and after T_{I2}; lines (2) and (3) are the characteristics of the jump from P_1 to P_2 and the draining front of P_2, respectively; line (4) is the interception function (that turns into the curved section of the wetting shock front after T_{I2}). Adapted with permission from Germann (2014). See also Fig. 5 for the KW expressions. A color version of this figure is available in the online version of this article.

T_{I1}, when the wetting shock front of P_1, line (1) in Fig. 8, intercepts the jump characteristic, line (2) in Fig. 8, and T_{I2}, when the wetting shock front from the combined P_1 and P_2 intercepts the draining from the last lamina of P_2, characteristic line (3) in Fig. 8.

The following presents the procedures of determining the two interception depths and times, the spatiotemporal position of the wetting shock front in the three intervals of (i) $[T_B \le \tau_1 \le T_{I1}]$, (ii) $[T_{I1} \le \tau_2 \le T_{I2}]$, (iii) $[\tau_3 \ge T_{I2}]$, and the associated mobile water contents.

(i) Interval $T_{B1} \le \tau_1 \le T_{I1}$

The wetting shock front of P_1 moves with v_{W1}, Eq. [7] and line (1) in Fig. 8. It intercepts the characteristic of the jump, Eq. [54] and line (2) in Fig. 8, at time and depth of T_{I1} and Z_{I1}. Solving the pair of linear equations of $Z_{I1} = (T_{I1} - T_{B1})\cdot v_{W1}$ and $Z_{I1} = (T_{I1} - T_{E1})\cdot c_{J12}$ yields

$$T_{I1} = \frac{T_{E1}\cdot c_{J12} - T_{B1}\cdot v_{W1}}{c_{J12} - v_{W1}} \quad [55]$$

$$Z_{I1} = c_{J12}\cdot v_{W1}\cdot\frac{T_{E1}-T_{B1}}{c_{J12}-v_{W1}} \quad [56]$$

The mobile water content at the wetting front during τ_1 is w_{S1} that also applies to the triangle between the surface, the wetting front, and the characteristic of the jump.

(ii) Interval $T_{I1} \le \tau_2 \le T_{I2}$

Beyond Z_{I1} and after T_{I1}, the wetting front moves with the velocity v_{W2} according to P_2, slope of line (1) in Fig. 8, with the characteristic of

$$z_W(\tau_2) = (\tau_2 - T_{B2a})\cdot v_{W2} \quad [57]$$

Again, the offset of T_{B2a}, Eq. [47], indicates the apparent earlier release of P_2 because of its gliding on P_1. The draining front of P_2 is released at T_{E2} with the characteristic of line (3) in Fig. 8. Line (3) is steeper than line (2), indicating that P_2 superimposes P_1. The wetting front of P_2, line (1) in Fig. 8, intercepts P_2's draining front at T_{I2} and Z_{I2}. Solving the pair of linear equations of $Z_{I2} = Z_{I1} + (T_{I2} - T_{I1})\cdot v_{W2}$ and $Z_{I2} = (T_{I2} - T_{E2})\cdot c_{D2}$, while recognizing that $c_{D2} = 3 \times v_{W2}$, yields

$$T_{I2} = \frac{1}{2}\cdot(3\cdot T_{E2} - T_{B2a}) \quad [58]$$

$$Z_{I2} = \frac{c_{D2}}{2}\cdot(T_{E2} - T_{B2a}) \quad [59]$$

The mobile water content at the wetting front is w_{S2} as well as in the spatiotemporal quadrangle between the surface, the characteristic of the jump, line (2); the wetting front, line (1); and the characteristic of the draining front, line (3).

(iii) Interval $\tau_3 \ge T_{I2}$

The interception function is released at T_{E2}, which appears as curved wetting front depth during τ_3, line (1) in Fig. 8. It progresses according to Eq. [21] as

$$z_W(\tau_3) = c_{D2}\cdot\left(\frac{T_{E2}-T_{B2a}}{2}\right)^{2/3}\cdot(\tau_3-T_{E2})^{1/3} \quad [60]$$

After passing of the draining front, the mobile water content decreases according to Eq. [27]. Alluding to Eq. [29], the mobile water content along the wetting front during τ_3, line (1) in Fig. 8, amounts to

$$w(\tau_3) = w_{S2}\cdot\left(\frac{T_{E2}-T_{B2}}{2\cdot(\tau_3-T_{E2})}\right)^{1/3} \quad [61]$$

TABLE 1. List of Symbols and Acronyms

Symbol/ Acronym	Dimension	Name
A	m^2	Cross-sectional area
AWI		Air-water interface
CF		Capillary flow
F	m	Film thickness
K	$m \cdot s^{-1}$	Hydraulic conductivity
KW		Kinematic wave
L	$m^2 \cdot m^{-3}$	Specific contact area per unit volume
P		Pulse
PF		Preferential flow
Re	—	Reynolds number
SWI		Solid-water interface
T_B	s	Time when pulse starts
T_{B2a}	s	Time offset due to earlier pulse
T_E	s	Time when pulse ends
T_I	s	Time of interception
VF		Viscous flow
V_{tot}	m	Total water volume of a WCW
V_{WCW}	m	Infiltrated water volume
WCW		Water content wave
Z_I	m	Depth of interception
b	$m \cdot s^{-1}$	Conductance
c	$m \cdot s^{-1}$	Celerity
c_D	$m \cdot s^{-1}$	Celerity of draining front
c_J	$m \cdot s^{-1}$	Jump celerity
df	m	Thickness of a lamina
f	m	Film thickness variable
g	$m \cdot s^{-2}$	Acceleration due to gravity
q	$m \cdot s^{-1}$	Volume flux density
q_S	$m \cdot s^{-1}$	Volume flux density of pulse
t	s	Time coordinate
t_{CR}	s	Time of the crest to move to z
t_D	s	Draining front time
t_W	s	Wetting front time
v_{CR}	$m \cdot s^{-1}$	Wetting shock front velocity at the crest
v_W	$m \cdot s^{-1}$	Velocity of wetting front
w	$m^3 \cdot m^{-3}$	Mobile water content
w_{CR}	$m^3 \cdot m^{-3}$	Mobile water content at the crest
z	m	Depth coordinate
z_D	m	Draining front depth
z_W	m	Wetting front depth
ζ	m	Local depth variable
η	$m^2 \cdot s^{-1}$	Kinematic viscosity
θ	$m^3 \cdot m^{-3}$	Volumetric water content
ρ	$kg \cdot m^{-3}$	Density
τ	s	Local time variable
φ	Pa	Shear force
ψ	Pa	Capillary potential

During τ_3, the mobile water content behind the wetting front evolves according to Eq. [31], where $w(\tau_3)$ from Eq. [61] replaces $w_{CR}(\zeta_2,t)$.

All volume flux densities follow from the mobile water contents according to Eq. [32]. The water balance calculations follow from Eq. [53].

Discussion of Characteristics (i.e., Trajectories) and Kinematic Waves

Kinematic wave theory provides a robust mathematical tool for routing wetting shock fronts originating from individual pulses that belong to extended time series. So far, the approach is limited to the macropore flow restriction, Eq. [35]; however, there is confidence in the development of experimental relationships of $L(q_S)$. The $w(z,t)$ and $q(z,t)$ values can be grafted on the temporal positions of the wetting shock fronts and draining fronts once the interception depths and times have been determined. Pulse routing remains robust also in the cases of either $w_1 = w_2$ or $w_2 = 0$, thus rendering even more flexibility to the modeling of PF (Table 1).

SUMMARY, DISCUSSION, AND CONCLUSIONS

Newton's (1729) law of shear is the base for momentum dissipation during laminar flow that evolves here as VF to the approaching of PF in permeable media. The concept exclusively uses analytical expressions that result in a set of stringent theoretical relationships completely expressing PF. Superfluous numerical procedures neither obscure the VF approach, nor do they introduce ambiguity. Thus, the spatiotemporal propagation of an input pulse depends only on the two parameters, film thickness F and specific contact area L, greatly facilitating calibration and application. Because viscosity continuously balances gravity, the concept of representative elementary volume, REV, is redundant. Therefore, scale restrictions of the spatiotemporal approach's applicability vanish. The WCW emerges as the basic unit of the spatiotemporal distribution of mobile water content that is due to the infiltration of a rectangular pulse. Analytical expressions define adequately the wave's projections onto the two planes of mobile water content versus time and depth, respectively. Further, the wave's projection onto the depth-time plane links the approach with the theory of KW according to Lighthill and Witham (1955). The link thus leads to the routing of input pulse series, each pulse with individual duration and intensity. The two-pulse examples provided in "Propagation of a Faster Pulse With Higher-Volume Flux Density That Superimposes (Overtakes) a Slower Pulse With Lower-Volume Flux Density" and "Discussion of Characteristics (i.e., Trajectories) and Kinematic Waves" extend to their respective limits of $q_{S1} = q_{S2}$, which greatly facilitates modeling of pulse series.

Already the assessment of the pulses' penetration depths indicates a wide spectrum of VF applications. For instance, shallow penetrations of short pulses are important in the optimization of irrigation schemes, whereas longer lasting pulses reaching greater depths are

important in groundwater recharge considerations. Thus, adaption to specific problems is simple because the approach applies to both situations without scale jump. From the approach's stringency follows that any deviations from water balance calculations, Eq. [53], are exclusively due to either methodological uncertainties or to deviations from VF and PF in view of this contribution. Methodological uncertainties set aside, too low a depth integral of mobile water content in comparison with the volume of infiltration indicates on the one hand flow divergence within a volume of the permeable medium that is considerably larger than the control volume occupied by the instrumentation. On the other hand, it may indicate water abstraction from the WCW due to capillarity. Observed deviations thus provide for a starting point for investigating interactions between the F und L parameters on one side and the spatiotemporal action of capillarity on the other side. Conversely, too high a depth integral of mobile water in the balance is indicative of flow converging from a volume of the permeable medium larger than the control volume of instrumentation. Investigating balance deviations due to flow divergence or convergence lead to spatial variability considerations of PF. Also, volume balance considerations in view of VF may help understanding nonequilibrium flow in Richards' (1931) CF (Germann, 2018a).

However, the VF approach to PF is limited to laminar flow as expressed with the Reynolds number, Eq. [8]. It is further restricted to gravity-driven flow, that is, close to the vertical-down direction. Thus, VF excludes a priori any capillary rise. For practical reasons, the macropore flow restriction, Eq. [35], has to be assumed as long as no relationships between volume flux density of input and L have been explored in more details.

Scientifically accepted theory and experimental procedures are available for the in situ determination of the VF parameters, film thickness F and specific contact area L (Germann, 2018b). Thus, the VF package just awaits to be used for addressing various PF problems. For example, the specific contact area L is considered the locus of momentum dissipation, exchange of heat, solutes, and particles between PF and the resting parts of the permeable medium. In particular, L seems the predestined parameter of abstraction from mobile water due to capillarity.

ACKNOWLEDGMENT

The editor-in-chief of Soil Science, Daniel Gimenez, invited the manuscript on hydromechanics and kinematics in PF. His and Tammo Steenhuis' comments greatly improved the revision.

REFERENCES

Beven K., and P. Germann. 1981. Water flow in soil macropores II. A combined flow model. J. Soil Sci. 32(1):15–29.

Darcy H. 1856. Les fontaines publiques de la ville de Dijon. Dalmont, Paris.

Dupuit J. 1863. Etudes théoriques et pratiques sur le mouvement des eaux dans les canaux découverts et à travers les terrains perméables. ((deuxième édition) ed.) Dunod, Paris.

Germann P. F. 1985. Kinematic wave approach to infiltration and drainage into and from soil macropores. Trans. ASAE. 28(3):745–749.

Germann P. F. 1986. Rapid drainage response to precipitation. Hydrol. Process. 1:2–13.

Germann P. F. 2014. Preferential Flow—Stokes Approach to Infiltration and Drainage. Geographica Bernensia, University of Bern, Bern, Switzerland.

Germann P. F. 2018a. Viscosity—the weak link between Darcy's law and Richards' (1931) capillary flow. Hydrol. Process. 32:1166–1172.

Germann P. F. 2018b. Preferential flow at the Darcy-scale: Parameters from water content time series. Methods Soil Anal. 3:160121.

Germann P. F., and S. A. al-Hagrey. 2008. Gravity-driven and viscosity-dominated infiltration into a full-scale sand model. Vadose Zone J. 7:1160–1169.

Germann P. F., and M. Karlen. 2016. Viscous-flow approach to in situ infiltration and in vitro hydraulic conductivity determination. Vadose Zone J. 15(12).

Germann P. F., and V. Prasuhn. 2017. Viscous flow approach to rapid infiltration and drainage in a weighing lysimeter. Vadose Zone J. 17:170020.

Germann P. F., W. M. Edwards, and L. B. Owens. 1984. Profiles of bromide and increased soil moisture after infiltration into soils with macropores. Soil Sci. Soc. Am. J. 48(2):237–244.

Harrold L. L., and F. R. Dreibelbiss. l958. Evaluation of agricultural hydrology by monolith lysimeters. *In:* USDA Tech. Bull. No. 1179, pp. 166.

Hincapié I. A., and P. Germann. 2009a. Abstraction from infiltrating water content waves during weak viscous flows. Vadose Zone J. 8:996–1003.

Hincapié I., and P. F. Germann. 2009b. Impact of initial and boundary conditions on preferential flow. J. Contam. Hydrol. 104:67–73.

Hincapié I. A., and P. Germann. 2010. Water content wave approach applied to neutron radiographs of finger flow. Vadose Zone J. 9:278–284.

Jarvis N., J. Koestel, and M. Larsbo. 2016. Understanding preferential flow in the vadose zone: Recent advances and future prospects. Vadose Zone J. 15(12).

Kelley G. P., W. M. Edwards, L. L. Harrold, and J. L. McGuiness. 1975. Soils of the North Appalachian Watershed. USDA Misc. Publ. No. 1296. U.S. Government Priniting Office, Washington, DC.

Lawes J. B., J. H. Gilbert, and R. Warington. 1882. On the amount and composition of the rain and drainage waters collected at Rothamsted. W. Clowes and Sons, Ltd., London.

Lighthill M. J., and G. B. Witham. 1955. On kinematic waves—I. Flood movement in long rivers. Proc. R. Soc. London Ser. A. 229:281–316.

Newton I. 1729. The Mathematical Principles of Natural Philosophy—Translation Into English. Vol. II. Benjamin Motte, London, UK, pp. 184.

Nimmo J. R. 2010. Theory of source-responsive and free-surface film modeling of unsaturated flow. Vadose Zone J. 9:295–306.

Nimmo J. R. 2012. Preferential flow occurs in unsaturated conditions. Hydrol. Process. 26:786–789.

Poiseuille J. L. M. 1846. Recherches expérimentales sur le mouvement des liquides dans les tubes de très petits diamètres. Comptes Rendus, xi-xii. Mém. des Sav. Etrangers, ix.

Richards L. A. 1931. Capillary conduction of liquids through porous mediums. Phys. Chem. Chem. Phys. 1:318–333.